2022 International Conference on Unmanned Aircraft Systems (ICUAS)
Dubrovnik, Croatia. June 21-24, 2022

Design and Characteristics of a New Transformable UAV with both Coplanar and Omnidirectional Features

Shi Lu, Armando Rodriguez, Konstantinos Tsakalis, and Yan Chen*

2022 International Conference on Unmanned Aircraft Systems (ICUAS) | 978-1-6654-0593-5/22/$31.00 ©2022 IEEE | DOI: 10.1109/ICUAS54217.2022.9836144

***Abstract*—To broaden and promote the applications of unmanned aerial vehicles (UAVs), UAVs with agile and omnidirectional mobility enabled by full or over actuation are a growing field of research. However, the balance of motion agility and force (energy) efficiency is challenging for a fixed UAV structure. This paper presents the new design of a transformable UAV, which can operate as a coplanar hexacopter or as an omnidirectional multirotor based on different operation modes. The UAV has 100% force efficiency for launching or landing tasks in the coplanar mode. In the omnidirectional mode, the UAV is fully actuated in the air for agile mobility in six degrees of freedom (DOFs). Models and control design are developed to characterize the motion of the transformable UAV. Simulation results are presented to validate the transformable UAV design and the enhanced UAV performance, compared with a fixed structure.**

I. Introduction

Industrial and agricultural unmanned aerial vehicles (UAVs) have been widely used for long-distance flight applications such as aerial photography, mapping, package transportation, inspection, and pesticide spraying during the last several decades [1][2][3]. Typically, coplanar multirotor UAVs, such as quadcopters and hexacopters, are applied to perform these tasks because of their carrying capacity and mechanical simplicity [8][13]. These UAVs primarily work at near-hovering equilibriums with the thrust vectors limited to a single direction. The coupled translational and rotational kinematics indicate dependent position and orientation control. However, independent control of all six degrees of freedom (DOFs) for new challenges in difficult tasks, such as complex aerial movement and manipulation [13][15][20][22], may require full actuation with more actuators onboard.

Various tilted arms were added to common multirotors to achieve full even over actuation. Over-actuation could potentially enhance the overall system energy efficiency by optimizing control allocation on different actuators, which was demonstrated on ground vehicles [4]. In [5]-[7], servo motors were added to rotate UAV arms independently around their main axes either radially or tangentially, and thus thrust vectors could be adjusted within certain limited angles in one plane to make the platform over-actuated. However, those platforms have low energy-efficiency issues for most movements due to internal force/torque cancellation. On the other hand, each arm of quadcopters was designed to rotate in $\mathbb{S}^2$ with two servo motors, which caused a problem of short flight time by using eight additional motors to tilt four arms [8][10]. Furthermore, in [11][12], coupled tiltable mechanism controlled by two servos was added to adjust directions of thrust vectors. Unlike the four-servo and the eight-servo solutions, these platforms could reduce or avoid energy dissipation issues. Due to the limitation of mechanical design and actuator constraints, although the platforms with tiltable arms increased force or energy efficiency with over-actuation, they cannot achieve omnidirectional motions.

Omnidirectional UAVs demonstrate advantages of aerial interaction, uninhibited observation, and better capability for complex aerial manipulation missions, compared with common coplanar UAVs [13]. Towards omnidirectional flight capability, platforms with fixed-motor configuration (and no tilt-arm servos) were developed based on optimization of static thrust and torque analysis in [13]-[15]. The force envelops must be larger than gravity in all directions with additional increments to maintain a hovering status [15]. Hence, at least six rotors allocated on at least three different planes are required. These platforms can exploit decoupled translational and rotational kinematics but suffer significant energy dissipation. By combining the idea of tiltrotor and omnidirectional fixed motor configuration, platforms in [15]-[17] could hover in any orientation while maintaining efficient flight configurations. However, the platform in [15] is still heavy and has a short flight time without a power tether, equipped with six tilt-arm servos and twelve rotors (two on each arm with opposite direction to generate bi-directional thrusts). The omnidirectional UAVs generally advance full-state flight capability but exhibit inherent limitations, such as overweight or significant energy dissipation. To achieve desired design weight and optimal energy efficiency with omnidirectional mobility, the number of the UAV actuators should be minimized.

Because coplanar UAVs typically have high energy efficiency, but with under-actuated configurations, a new trend of UAV design is to combine features of coplanar UAVs with full actuation [20]. Although the platform could transit between an under-actuated coplanar mode and a fully actuated non-coplanar mode with one servo motor, which reduced energy consumption and design weight, the UAV lacked the capability of omnidirectional motions and extended manipulation capability based on omnidirectional motions.

Motivated by the combined advantages of coplanar and omnidirectional UAVs, which can enable a broader range of applications, the first contribution of this paper is to present a new transformable UAV platform by integrating both coplanar and omnidirectional motion features. Reversible motors [21] with little nonlinearity influence (dead zone and delay at zero crossing) are selected to generate bidirectional thrusts instead

*Corresponding Author. Shi Lu (e-mail: shilu@asu.edu), Armando Rodriguez (e-mail: aar@asu.edu), and Konstantinos Tsakalis (e-mail: tsakalis@asu.edu) are with School for Electrical, Computer and Energy Engineering, Arizona State University, AZ, USA. Yan Chen is with the Polytechnic School, Arizona State University, AZ, USA (e-mail: yanchen@asu.edu).

of dual motors placed in an opposite direction with heavier weights. The transformation mechanism is designed by using only one servo motor with a driving mechanism to transform between the coplanar (under-actuated) mode and the omnidirectional (fully-actuated) mode. The second contribution is to model and control the transformable UAV with improved mobility performance. In the coplanar mode, the UAV can operate in $\mathbb{R}^3$ as an under-actuated hexacopter without energy dissipation. In the omnidirectional mode, the UAV can track a full pose trajectory in $\mathbb{R}^3 \times SO(3)$ as a fully actuated system. This platform can arbitrarily transform for the required missions, e.g., long-range agile flight or complicated aerial manipulation.

The paper is structured as follows. The transformable UAV design and mathematical models are introduced in Section II. A full-pose geometry control in $\mathbb{R}^3 \times SO(3)$ is presented in Section III. The simulation results show the design validity and control performance in Section IV. Finally, we conclude the paper with an outline of future work in Section V.

II. Modeling of The Transformable UAV

In this section, the UAV mechanical design is reviewed first in subsection A. In subsection B, the actuator model and analysis of the efficiency index are introduced. In subsection C, the rigid body model and force efficiency are presented.

A. UAV Design

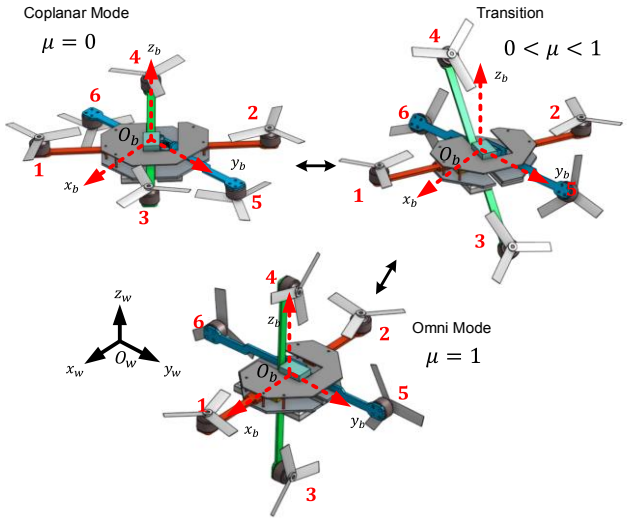

Fig. 1. Design and Schematics of a Transformation UAV.

The concept of a transformable UAV is shown in Fig. 1. The UAV has six reversible rotors, and three arms are respectively depicted in red, green, and blue colors, generating thrusts normal to the plane in the coplanar mode. Here we define the inertial reference frame $\mathcal{F}_w = O_w, \{\boldsymbol{x}_w, \boldsymbol{y}_w, \boldsymbol{z}_w\}$ and the body frame $\mathcal{F}_b = O_b, \{\boldsymbol{x}_b, \boldsymbol{y}_b, \boldsymbol{z}_b\}$. O_b corresponds to the center of the body frame and the center of mass. In the coplanar mode, all six rotors are located at the same plane, and all rotor disk norms are parallel to the $\boldsymbol{z}_b$ axis. During the transition, the green arm (rotor 3, 4) and the blue arm (rotor 5, 6) rotate around the center of the red arm (rotor 1, 2) with a direction change of $\boldsymbol{x}_b$ (in the body frame). In omnidirectional mode, six rotors are located at the vertices of a regular octahedron [13].

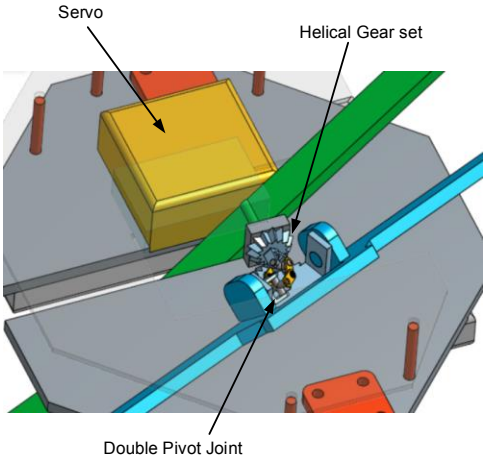

Fig. 2. Mechanical Design of the Transformation Mechanism.

We denote the three canonical rotation matrices [13] in $SO(3)$ with $\boldsymbol{R}_x$, $\boldsymbol{R}_y$, and $\boldsymbol{R}_z$, and the operating mode of the transformable UAV with $\mu \in [0, 1]$. We define $\mu = 0$ for the coplanar mode, $\mu \in (0,\ 1)$ for the transition state, and $\mu = 1$ for the omnidirectional mode. The position and disk normal of all six motors are given by

$$\begin{aligned}
\boldsymbol{P} &= [\boldsymbol{R}_1(\mu)\boldsymbol{p}_{1,0} \quad \boldsymbol{R}_2(\mu)\boldsymbol{p}_{2,0} \quad \cdots \quad \boldsymbol{R}_6(\mu)\boldsymbol{p}_{6,0}] \\
\boldsymbol{N} &= [\boldsymbol{R}_1(\mu)\boldsymbol{n}_{1,0} \quad \boldsymbol{R}_2(\mu)\boldsymbol{n}_{2,0} \quad \cdots \quad \boldsymbol{R}_6(\mu)\boldsymbol{n}_{6,0}] \\
\boldsymbol{p}_{1,0} &= -\boldsymbol{p}_{2,0} = \left[\tfrac{\sqrt{2}}{2}l \quad -\tfrac{\sqrt{2}}{2}l \quad 0\right]^T \\
\boldsymbol{p}_{3,0} &= -\boldsymbol{p}_{4,0} = \left[\tfrac{\sqrt{2}}{2}l \quad \tfrac{\sqrt{2}}{2}l \quad 0\right]^T \\
\boldsymbol{p}_{5,0} &= -\boldsymbol{p}_{6,0} = [0 \quad l \quad 0]^T \\
\boldsymbol{n}_{1,0} &= \boldsymbol{n}_{2,0} = \boldsymbol{n}_{3,0} = \boldsymbol{n}_{4,0} = [0\ 0\ 1]^T \\
\boldsymbol{n}_{5,0} &= \boldsymbol{n}_{6,0} = [0\ 0\ -1]^T
\end{aligned} \quad , \tag{1}$$

where $\boldsymbol{p}_{i,0}$ $(i = 1, \cdots, 6)$ is the rotor position relative to the UAV geometric center in the coplanar mode. Each rotor has the same distance l from the geometric center. The red and the green arms in Fig. 1 are mutually perpendicular. The blue arm has a 45-degree angle with the other two arms and coincides $\boldsymbol{y}_b$. The 45 degrees and 90 degrees are intentionally selected as the arm intersection angles for a direct and simple mechanical transformation towards the omni-mode as shown in Fig. 1. Furthermore, $\boldsymbol{n}_{i,0}$ $(i = 1, \cdots, 6)$ are disk normal of six rotors in the coplanar mode. Let $\boldsymbol{p}_i = \boldsymbol{R}_i\boldsymbol{p}_{i,0}$ and $\boldsymbol{n}_i = \boldsymbol{R}_i\boldsymbol{n}_{i,0}$. Then the rotation transition expression of each rotor $\boldsymbol{R}_i$ $(i = 1, \cdots, 6)$ is given by

$$\begin{cases}
\boldsymbol{R}_1(\mu) = \boldsymbol{R}_2(\mu) = \boldsymbol{R}_z\left(\mu\frac{\pi}{4}\right) \\
\boldsymbol{R}_3(\mu) = \boldsymbol{R}_4(\mu) = \boldsymbol{R}_x\left(\mu\frac{\pi}{2}\right)\boldsymbol{R}_z\left(\mu\frac{\pi}{4}\right) \\
\boldsymbol{R}_5(\mu) = \boldsymbol{R}_6(\mu) = \boldsymbol{R}_y\left(\mu\frac{\pi}{2}\right)
\end{cases}. \tag{2}$$

The transformation mechanism is designed in Fig. 2. The servo directly rotates the green arm. The helical gear is attached to the green arm, and the pivot joint acts at the blue arm. During the transition, the angle between the heading axis $\boldsymbol{x}_b$ and the red arm varies from 0 to 45 degree. A swift transition will be limited to avoid introducing unnecessary disturbances, and further discussions are given in subsections B and C. The transition time is designed within two seconds.

The UAV will operate in either the coplanar or the omnidirectional mode.

B. Actuator Model & Efficiency Analysis

Most UAVs use unreversible motors plus ESCs, in which one single rotor thrust is constrained to

$$0 < f_{\text{rotor,min}} \leq f_{\text{rotor}} \leq f_{\text{rotor,max}}. \tag{3}$$

To generate a bi-directional thrust, two motors are placed in an opposite direction in some omnidirectional design [15][22], which causes large weights and energy loss. To overcome this issue, we choose well-designed reversible motors [21] with symmetric propellers, giving one single rotor-propeller thrust constrained to

$$-f_{\text{rotor,max}} = f_{\text{rotor,min}} \leq f_{\text{rotor}} \leq f_{\text{rotor,max}}. \tag{4}$$

The dead zone effect can be ignored since $\min(|f_{\text{rotor}}|) < 0.01\text{N}$. With reversible motors, symmetric propellers, and suitable total weight, the omnidirectional flight is achievable with two motors supplying most of the thrust to overcome the gravity, similar to the capability of other omnidirectional UAV studies [21]. The thrust f_{rotor} and inverse torque τ_{rotor} of each rotor are introduced and simplified as

$$\begin{aligned} f_{\text{rotor},i} &= \text{sgn}(\omega_i) k_f \omega_i^2 \\ \tau_{\text{rotor},i} &= k_{\tau-f} f_{\text{rotor},i} \end{aligned} \quad i = 1,2 \cdots 6. \tag{5}$$

where ω is the rotor speed, and k_f and $k_{k_{\tau-f}}$ are aerodynamic factors of the rotors and the surrounding air, respectively. To simplify the actuator dynamics, the transfer function between the desired thrust $f_{\text{rotor,des}}$ and actual thrust f_{rotor} as a first-order low-pass filter

$$f_{\text{rotor}} = \frac{a}{s+a} f_{\text{rotor,des}}. \tag{6}$$

The total thrust $\boldsymbol{F}_{3\times1}$ and torque $\boldsymbol{T}_{3\times1}$ is given by

$$\begin{bmatrix} \boldsymbol{F} \\ \boldsymbol{T} \end{bmatrix} = \begin{bmatrix} \boldsymbol{N} \\ \boldsymbol{P} \times \boldsymbol{N} \end{bmatrix} \boldsymbol{f}_{\text{rotor}} + \begin{bmatrix} \boldsymbol{0}_{3\times6} \\ \boldsymbol{N}_{\boldsymbol{\tau}} \end{bmatrix} \boldsymbol{\tau}_{\text{rotor}}. \tag{7}$$

Here thrust $\boldsymbol{f}_{\text{rotor}} = [f_{\text{rotor},1}, f_{\text{rotor},2}, \cdots f_{\text{rotor},6}]^T$, inverse torque $\boldsymbol{\tau}_{\text{rotor}} = [\tau_{\text{rotor},1}, \tau_{\text{rotor},2}, \cdots \tau_{\text{rotor},6}]^T$ and the i-th column of $\boldsymbol{P} \times \boldsymbol{N}$ is $\boldsymbol{p}_i \times \boldsymbol{n}_i$ based (1). We have $\boldsymbol{N}_\tau = [-\boldsymbol{n}_1, \boldsymbol{n}_2, \boldsymbol{n}_3, -\boldsymbol{n}_4, \boldsymbol{n}_5, -\boldsymbol{n}_6]$ which denotes the motor direction allocation for yaw motion in coplanar mode. Substituting (5) into (7), force and torque expressions in (7) can be rewritten as

$$\begin{bmatrix} \boldsymbol{F} \\ \boldsymbol{T} \end{bmatrix} = \begin{bmatrix} \boldsymbol{N} \\ \boldsymbol{P} \times \boldsymbol{N} + k_{\tau-f} \boldsymbol{N}_\tau \end{bmatrix} \boldsymbol{f}_{\text{rotor}} = \boldsymbol{A} \boldsymbol{f}_{\text{rotor}}. \tag{8}$$

For different μ that correspond to different modes or transition, we have:

$$\begin{aligned} \mu = 0 &\Rightarrow \text{rank}(\boldsymbol{A}(\mu)) = 4, \ \boldsymbol{F} = [0\ 0\ F_z]^T \\ \mu \in (0,1] &\Rightarrow \text{rank}(\boldsymbol{A}(\mu)) = 6, \ \boldsymbol{F} = [F_x\ F_y\ F_z]^T. \end{aligned} \tag{9}$$

After the actuators are modeled, the rotor electrical power consumption is evaluated. An experiment using a reversible motor [21] with a 5045 symmetric propeller was conducted. The rotor thrust vs. electrical power curve fitting is shown in Fig. 3. A cubic polynomial model was developed in (10).

$$\begin{aligned} P_{\text{rotor}} &= k_{p1} f_{rotor}^3 + k_{p2} f_{rotor}^2 + k_{p3} f_{\text{rotor}} + k_{p4} \\ k_{p1} &= -3.736 \cdot 10^{-4},\ k_{p2} = 3.004 \\ k_{p3} &= 17.56,\ k_{p4} = 2.026 \end{aligned} \quad . \tag{10}$$

It is worth noting that $\dot{P}_{\text{rotor}} > 0$ for any reasonable $f_{\text{rotor}} \geq 0$. Thus, more energy will be cost if fewer actuators are selected to generate the same total thrust, which indicates the omni-mode costs more power than the coplanar mode at hovering.

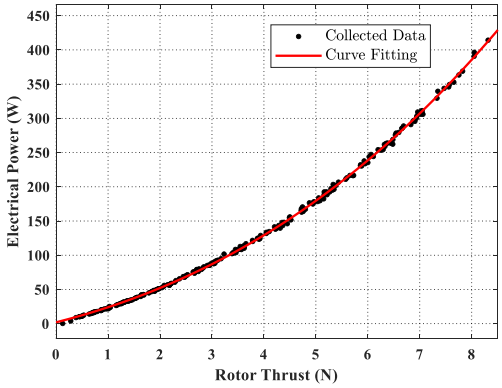

Fig. 3. An Empirical Model of Motor Electrical Power vs. Thrust.

In the coplanar mode, disk norms of six rotors are all collinear. The system works as an underactuated hexacopter with internal forces equal to zero during hovering. Yaw movement relies on the drag moment of each rotor. The system is fully actuated with internal forces determined by the current hovering orientation and transition state in the transition and omnidirectional mode. Based on [15][17][20], we adopted the idea of the force efficiency index:

$$\gamma(\mu, \boldsymbol{f}_{\text{rotor}}) = \frac{\|\boldsymbol{F}\|}{\Sigma_{i=1}^{6} |f_{\text{rotor,i}}|} \in [0,1]. \tag{11}$$

Clearly, $\gamma(\mu = 0, \boldsymbol{f}_{\text{rotor}}) = 1$ corresponds to the maximum force or energy efficiency.

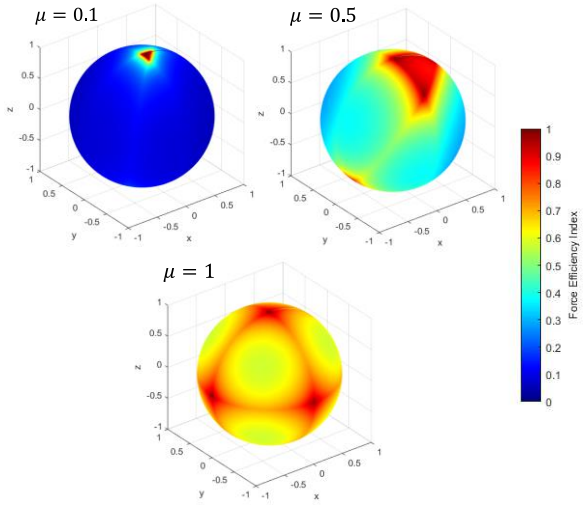

Fig. 4. Force Efficiency Index Map for $\mu \in (0,1]$.

The thrust vector coincides $\boldsymbol{z}_b$ without any remnant in $\boldsymbol{x}_b$ and $\boldsymbol{y}_b$ directions. Hence, the UAV has four controllable degrees of freedom (3D position plus yaw angle). The force

index maps corresponding to different $\mu \in (0,1]$ are shown in Fig. 4. The UAV is fully actuated but can only enter the omnidirectional mode after the transformation. All three subplots have $\gamma = 1$ at $\boldsymbol{z}_b$ in the positive direction. When μ is small, most of the efficiency index map is smaller than 0.5. Two main points are discussed as follows. 1) The UAV should not generate any force in the direction of $\boldsymbol{x}_b$ and $\boldsymbol{y}_b$ as the efficiency index is too low. The UAV needs to maintain low speed in transition and adds saturation on control inputs of rotors 3-6 at the early stage of transition. 2) To enter the omnidirectional mode or vice versa, the transition time is smooth enough to avoid unnecessary mechanical disturbances. As μ increases, we can see the overall efficiency index keeps increasing. When $\mu = 1$, the UAV fully enters the omnidirectional mode. The efficiency index is between 57.7% and 100%. It reaches 100% (no internal forces) at each axis, corresponding to the maximum power efficiency matching six sets of roll-pitch angles during flight. Such orientations should be applied during hovering to maximize the flight time in the omni-mode.

C. Rigid Body Model

We derive the rigid body kinematic model by considering the aerodynamic effects (interference) between rotors as disturbances. The inertial frame and the body frame are defined in subsection A. The UAV translational dynamics are described by the position $\boldsymbol{p} = [p_x\ p_y\ p_z]^T$ and the velocity $\boldsymbol{v} = [v_x\ v_y\ v_z]^T$. $\boldsymbol{g} = [0\ 0\ g]^T$ is the gravity vector, and $\boldsymbol{F}, \boldsymbol{T}$ are defined in (8). Based on [23][24], $\boldsymbol{R}$ is the rotation matrix maps from the body frame to the inertial frame, and $\boldsymbol{\omega} = [\omega_x\ \omega_y\ \omega_z]^T$ denotes the vehicle body angular velocity with the $\wedge$ operator converting $\boldsymbol{\omega}$ into $\boldsymbol{\omega}_\wedge$. Then we denote the translational (force) and rotational (torque) aerodynamic drag equations

$$\boldsymbol{F}_v = \begin{bmatrix} \mathrm{sgn}(v_x) C_v v_x^2 \\ \mathrm{sgn}(v_y) C_v v_y^2 \\ \mathrm{sgn}(v_z) C_v v_z^2 \end{bmatrix}$$
$$\boldsymbol{\tau}_\omega = \begin{bmatrix} \mathrm{sgn}(\omega_x) C_\omega \omega_x^2 \\ \mathrm{sgn}(\omega_y) C_\omega \omega_y^2 \\ \mathrm{sgn}(\omega_z) C_\omega \omega_z^2 \end{bmatrix}. \quad (12)$$

C_v, C_ω are drag coefficients. And we let $\boldsymbol{\tau}_s$ represents the inverse torque generated from the mechanical structure in transition. The center of gravity is not essentially changed since the transition mechanism is located in the center of the frame, and all modules are placed symmetrically. Summing all torque and thrust contributions and using the Newton-Euler approach, the equation of motion of the transformable UAV is expressed as

$$\begin{cases} \dot{\boldsymbol{p}} = \boldsymbol{v} \\ m\dot{\boldsymbol{v}} = -m\boldsymbol{g} + \boldsymbol{R}\boldsymbol{F} - \boldsymbol{F}_v \\ \dot{\boldsymbol{R}} = \boldsymbol{R}\boldsymbol{\omega}_\wedge = \boldsymbol{R}\begin{bmatrix} 0 & -\omega_z & \omega_y \\ \omega_z & 0 & -\omega_x \\ -\omega_y & \omega_x & 0 \end{bmatrix}, \\ \boldsymbol{J}\dot{\boldsymbol{\omega}} = -\boldsymbol{\omega} \times \boldsymbol{J}\boldsymbol{\omega} + \boldsymbol{T} - \boldsymbol{\tau}_\omega - \boldsymbol{\tau}_s \end{cases} \quad (13)$$

where m is the mass of the UAV and $\boldsymbol{J}$ is the 3×3 inertia tensor matrix. Then we denote $\boldsymbol{J}_{\text{arm }3-4}$, $\boldsymbol{J}_{\text{arm }5-6}$,and $\boldsymbol{J}_{\text{rest}}$ as the inertia tensor matrices of the green arm, blue arm, and the rest of the body parts, respectively. We also denote $\boldsymbol{J}_{\text{arm }3-4,0}$, $\boldsymbol{J}_{\text{arm }5-6,0}$ and $\boldsymbol{J}_{\text{rest},0}$ as inertia tensor matrices of all these body parts when $\mu = 0$. Thus, we can have

$$\begin{aligned} \boldsymbol{J} &= \boldsymbol{J}_{\text{arm }3-4} + \boldsymbol{J}_{\text{arm }5-6} + \boldsymbol{J}_{\text{rest}} \\ \boldsymbol{J}_{\text{arm }3-4} &= \boldsymbol{R}_x\left(\mu\tfrac{\pi}{2}\right)\boldsymbol{R}_z\left(\mu\tfrac{\pi}{4}\right)\boldsymbol{J}_{\text{arm }3-4,0} \\ \boldsymbol{J}_{\text{arm }5-6} &= \boldsymbol{R}_y\left(\mu\tfrac{\pi}{2}\right)\boldsymbol{J}_{\text{arm }5-6,0} \\ \boldsymbol{J}_{\text{rest}} &= \boldsymbol{R}_z\left(\mu\tfrac{\pi}{4}\right)\boldsymbol{J}_{\text{rest},0} \\ \boldsymbol{\tau}_s &= \left(\boldsymbol{J}_{\text{arm }3-4}\boldsymbol{R}_z\left(\mu\tfrac{\pi}{4}\right)\begin{bmatrix}\frac{\pi}{2}\\0\\0\end{bmatrix} + \boldsymbol{J}_{\text{arm }5-6}\begin{bmatrix}0\\\frac{\pi}{2}\\0\end{bmatrix}\right)\ddot{\mu} \end{aligned} \quad (14)$$

Based on (8) and (13), the equation of acceleration and rotation can be compactly rewritten as:

$$\begin{bmatrix} m\ddot{\boldsymbol{p}} \\ \boldsymbol{J}\dot{\boldsymbol{\omega}} \end{bmatrix} = -\begin{bmatrix} m\boldsymbol{g} + \boldsymbol{F}_v \\ \boldsymbol{\omega} \times \boldsymbol{J}\boldsymbol{\omega} + \boldsymbol{\tau}_\omega + \boldsymbol{\tau}_s \end{bmatrix} + \boldsymbol{B}\boldsymbol{f}_{\text{rotor}}$$
$$\boldsymbol{B} = \begin{bmatrix} \boldsymbol{R}\boldsymbol{N} \\ \boldsymbol{P} \times \boldsymbol{N} + k_{\tau-f}\boldsymbol{N}_{\boldsymbol{\tau}} \end{bmatrix}, \quad (15)$$

where $\boldsymbol{B}$ has the same rank as $\boldsymbol{A}$. Unlike [20], the UAV only performs tasks either as a coplanar underactuated hexacopter or as an omnidirectional multirotor with rotors located at the vertices of a regular octahedron.

III. Control Design

In this section, we introduce a switching control structure on $\mathrm{SO}(3)$ for the UAV model in Section II. The stability Fig. 5 shows the overall control architecture. To avoid low force efficiency along x, y axis as $\mu \leq 0.5$, the controller switching is performed at $\mu = \mu_0 > 0.5$, similar to the idea in [20]. In the coplanar mode, translational and rotational dynamics are coupled. Heading direction (yaw angle) and position tracking are achieved in a coupled loop. First, the position controller calculates desired rotation matrix and a total thrust at $\boldsymbol{z}_b$. The attitude controller subsequently outputs desired torques. Finally, the rotor thrust is chosen. In the transition state and omnidirectional mode, translational and rotational dynamics are decoupled, and hence the orientation and position are tracked in two separate loops. Based on [24], all controllers are designed with cascade PI/PD architecture.

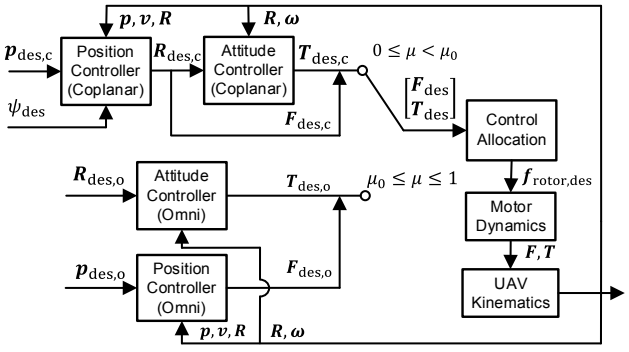

Fig. 5. Control Architecture.

A. Attitude Control

We assume the measurements are well filtered, and the attitude controller has a high sampling frequency. The attitude

controller is designed with a cascade geometric structure on $SO(3)$ which gives a smooth movement trajectory to track. The inner loop uses $\boldsymbol{\omega}$ as feedback to compute the reference torque based on feedback linearization [28] as

$$\boldsymbol{T}_{\text{des}} = -\boldsymbol{J}\left(\boldsymbol{k}_{p,\boldsymbol{\omega}}\boldsymbol{e}_{\boldsymbol{\omega}} + \boldsymbol{k}_{d,\boldsymbol{\omega}}\dot{\boldsymbol{e}}_{\boldsymbol{\omega}}\right) + \boldsymbol{\omega} \times \boldsymbol{J}\boldsymbol{\omega}, \tag{16}$$

which denotes a PD controller to deal with dynamics of angular velocity acting like a first-order system brought by motor dynamics in the actuator model. $\boldsymbol{k}_{p,\boldsymbol{\omega}}$, $\boldsymbol{k}_{d,\boldsymbol{\omega}}$ are positive gain matrices and $\boldsymbol{e}_{\boldsymbol{\omega}}$ is the angular rate error which is defined as

$$\begin{cases} \boldsymbol{e}_{\boldsymbol{\omega}} = \boldsymbol{\omega} - \boldsymbol{\omega}_{\text{des}} \\ \dot{\boldsymbol{e}}_{\boldsymbol{\omega}} = \dot{\boldsymbol{\omega}} - \dot{\boldsymbol{\omega}}_{\text{des}} \end{cases}. \tag{17}$$

The reference angular velocity is chosen as

$$\boldsymbol{\omega}_{\text{des}} = -\boldsymbol{k}_{p,\boldsymbol{R}}\boldsymbol{e}_{\boldsymbol{R}} - \boldsymbol{k}_{i,\boldsymbol{R}} \int \boldsymbol{e}_{\boldsymbol{R}}, \tag{18}$$

which is a PI controller. $\boldsymbol{k}_{p,\boldsymbol{R}}$ and $\boldsymbol{k}_{i,\boldsymbol{R}}$ are positive gain matrices, and $\boldsymbol{e}_{\boldsymbol{R}}$ is the orientation tracking error on $SO(3)$ defined as

$$\boldsymbol{e}_{\boldsymbol{R}} = \frac{1}{2}(\boldsymbol{R}_{\text{des}}^{T}\boldsymbol{R} - \boldsymbol{R}^{T}\boldsymbol{R}_{\text{des}})^{\vee}. \tag{19}$$

Based on [23], $\vee$ is the inverse operator of $\wedge$ in Eqn. (13). This attitude controller has the same structure in both working modes (coplanar/omnidirectional). The geometric control law gives exponential stability when the attitude tracking error should be less than $180°$. A low pass prefilter is added to the global attractiveness command signal.

B. Position Control

Similar to attitude controllers, position controllers are designed with a cascade structure. In coplanar mode, the position controller takes the yaw angle ψ_{des} and $\boldsymbol{p}_{\text{des}}$ as the reference trajectory. In the omnidirectional mode, the position controller takes $\boldsymbol{R}_{\text{des}}$ and $\boldsymbol{p}_{\text{des}}$ (full pose) as the reference trajectory. In both modes, we start by defining the outer loop

$$e_{\boldsymbol{p}} = \boldsymbol{p} - \boldsymbol{p}_{\text{des}}, \tag{20}$$

and use proportional control to get the desired velocity

$$\boldsymbol{v}_{\text{des}} = -\boldsymbol{k}_{p,\boldsymbol{p}}\boldsymbol{e}_{\boldsymbol{p}} - \boldsymbol{k}_{i,\boldsymbol{p}} \int \boldsymbol{e}_{\boldsymbol{p}}. \tag{21}$$

The velocity tracking error is defined as

$$\begin{cases} \boldsymbol{e}_{\boldsymbol{v}} = \boldsymbol{v} - \boldsymbol{v}_{\text{des}} \\ \dot{\boldsymbol{e}}_{\boldsymbol{v}} = \dot{\boldsymbol{v}} - \dot{\boldsymbol{v}}_{\text{des}} \end{cases}. \tag{22}$$

The desired force vector [27] in the inertial frame is defined as

$$\boldsymbol{F}_{\text{des,w}} = m\boldsymbol{g} - \left(\boldsymbol{k}_{p,\boldsymbol{v}}\boldsymbol{e}_{\boldsymbol{v}} + \boldsymbol{k}_{d,\boldsymbol{v}}\dot{\boldsymbol{e}}_{\boldsymbol{v}}\right), \tag{23}$$

which needs to be converted to the body frame. $\boldsymbol{k}_{p,\boldsymbol{p}}$, $\boldsymbol{k}_{i,\boldsymbol{p}}$, $\boldsymbol{k}_{p,\boldsymbol{v}}$, and $\boldsymbol{k}_{d,\boldsymbol{v}}$ are all positive definite diagonal matrices. The body heading axis in [23] needs to be calculated in the coplanar mode given the desired yaw angle. Hence, we first calculate the normalized thrust vector of the inertial frame

$$\hat{\boldsymbol{n}} = \boldsymbol{F}_{\text{des,w}} \Big/ \left\|\boldsymbol{F}_{\text{des,w}}\right\| = [n_1,\ n_2,\ n_3]^{T}, \tag{24}$$

based on the expression of the rotation matrix defined in modeling. Here we denote $\cos(\sin^{-1}(n_1))$ as n_4 and we have

$$\boldsymbol{R}_{\text{y,h}} = \begin{bmatrix} n_4 & 0 & n_1 \\ 0 & 1 & 0 \\ -n_1 & 0 & n_4 \end{bmatrix}, \tag{25}$$

if $n_4 = 0$ marking the singularity, then denote $\boldsymbol{R}_{\text{x,h}} = \boldsymbol{I}_{3\times 3}$. Otherwise, we have

$$\boldsymbol{R}_{\text{x,h}} = \begin{bmatrix} 1 & 0 & 0 \\ 0 & n_3/n_4 & n_2/n_4 \\ 0 & -n_2/n_4 & n_3/n_4 \end{bmatrix}. \tag{26}$$

Let $\boldsymbol{u} = \boldsymbol{R}_{\text{x,h}}\boldsymbol{R}_{\text{y,h}}\boldsymbol{R}_{z}(\psi_{\text{ref}}) \cdot [0,0,1]^{T}$ and $\hat{\boldsymbol{u}} = \boldsymbol{u}/\|\boldsymbol{u}\|$. Then denote $\hat{\boldsymbol{k}} = \boldsymbol{n} \times \boldsymbol{u}/\|\boldsymbol{n} \times \boldsymbol{u}\|$. Finally, we have the reference rotation matrix in coplanar mode

$$\boldsymbol{R}_{\text{des,c}} = \left[\hat{\boldsymbol{u}}\ \hat{\boldsymbol{k}}\ \hat{\boldsymbol{n}}\right]. \tag{27}$$

In the omnidirectional mode, $\boldsymbol{R}_{\text{des,o}}$ is the reference input. Hence, the reference force in the body frame is given by

$$\boldsymbol{F}_{\text{des}} = \boldsymbol{R}^{T}\boldsymbol{F}_{\text{des,w}}, \tag{28}$$

in both modes. Notice $\boldsymbol{F}_{\text{des.c}} = \left[0\ 0\ F_{\text{z,c}}\right]^{T}$ in the coplanar mode, and $\boldsymbol{F}_{\text{des,o}} = \left[F_{\text{x,o}}\ F_{\text{y,o}}\ F_{\text{z,o}}\right]^{T}$ in the omnidirectional mode. The position control in both modes has a similar pattern with [23] which is asymptotically stable.

C. Control Allocation

To obtain the unique relation for minimization of control effort, the reference force and torque are converted to rotor thrust with a pseudo-inverse [13] of the allocation matrix, which is

$$\boldsymbol{M} = \boldsymbol{A}^{T}(\boldsymbol{A}\boldsymbol{A}^{T})^{-1}. \tag{29}$$

Then, the reference rotor thrust can be computed by

$$\boldsymbol{f}_{\text{rotor,com}} = \boldsymbol{M}\begin{bmatrix} \boldsymbol{F}_{\text{des}} \\ \boldsymbol{T}_{\text{des}} \end{bmatrix}. \tag{30}$$

IV. Simulation Results and Discussions

This section presents simulation scenarios in MATLAB and results to illustrate the enhanced performance of the designed transformable UAV. A list of chosen modeling parameters in simulation is shown in Table 1, and a list of controller parameters is shown in Table 2.

Table 1. Model parameters of the transformable UAV in simulations

Symbol	Definition	Value
m	Total mass	0.945 kg
l	Distance between rotors and O_b	0.16 m
$\boldsymbol{J}_{\text{arm 3-4,0}}$	Inertia tensor matrix of the green arm at $\mu = 0$	$\begin{bmatrix} 0.0008 & -0.0005 & 0 \\ -0.0004 & 0.0009 & 0 \\ 0 & 0 & 0.0016 \end{bmatrix}$ kg · m^2
$\boldsymbol{J}_{\text{arm 5-6,0}}$	Inertia tensor matrix of the blue arm at $\mu = 0$	$\begin{bmatrix} 0.0015 & 0 & 0 \\ 0 & 0.0004 & 0 \\ 0 & 0 & 0.0018 \end{bmatrix}$ kg · m^2
$\boldsymbol{J}_{\text{rest,0}}$	Inertia tensor matrix of rest parts at $\mu = 0$	$\begin{bmatrix} 0.0024 & 0.0005 & 0 \\ 0.0004 & 0.0016 & 0 \\ 0 & 0 & 0.0072 \end{bmatrix}$ kg · m^2
μ_0	Controller switching flag	0.8

g	Gravity acceleration	9.81 m/s^2
a	Rotor dynamics coefficient	9
$f_{\text{rotor,max}}$	Rotor max thrust	8.5 N
k_f	Rotor thrust coefficient	$1.21 \cdot 10^{-6}$ N/rad^2
$k_{\tau-f}$	Rotor thrust to torque coefficient	0.012 m
C_v	Translational Drag Coefficient	0.25 N $\cdot$ s^2/m^2
C_ω	Rotational Drag Coefficient	0.005 N $\cdot$ m $\cdot$ s^2/rad^2

A. *Simulation Scenario*

The most challenging and significant mission for the transformable UAV is the combined flight containing under-actuated long-range flight and omnidirectional motions in the air. The commanded trajectory consists of three phases, and the 2-second transitions happen between two phases:

1) Phase 1 ($0 \le t < 16$ s): The UAV is first commanded to take off, accelerate, and fly to a long-distance set point as a coplanar hexacopter. The vehicle decelerates as the UAV approaches the destination, and the transition begins.

2) Transition C $\rightarrow$ O ($16 \le t < 18$ s): The UAV transforms from the coplanar mode to the omnidirectional mode at a suitable translational speed, and then the system becomes fully actuated.

3) Phase 2 ($18 \le t < 42$ s): The UAV enters the omnidirectional mode. In real applications, sinusoidal signals are used to generate reference 3D positional tracking with steer attitude ($18 \le t < 30$ s) and 3D rotational tracking with steer position ($30 \le t < 42$ s) separately, representing two different aerial tasks, such as aerial writing [29] and inspection, respectively.

4) Transition O $\rightarrow$ C ($42 \le t < 44$ s): The UAV transforms from the omnidirectional mode back to the coplanar directional mode at a suitable translational speed, and the system becomes under actuated again.

5) Phase 3 ($44 \le t < 60$ s): The UAV accelerates and flies towards the landing area. As the UAV approaches the target area, the vehicle velocity reduces, and the UAV finally finishes the landing.

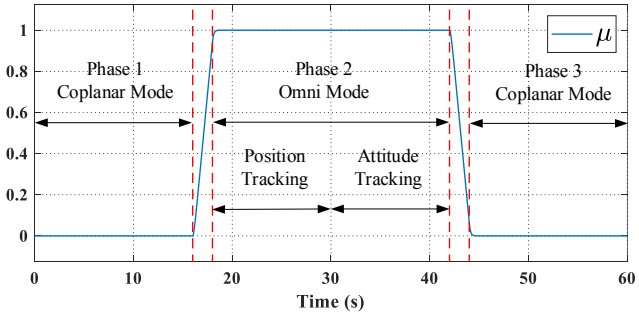

Fig. 6. The Flight Mode Switching.

Fig. 6 shows the mode (μ) switching plot. To describe the servo and the rotational structure dynamics during the transition associated with μ, a saturated damping signal is selected by going through a first-order low pass filter ($G_{LP} = \frac{\omega_0}{s+\omega_0}$, $\omega_0 \cong 6$ rad/s).

Table 2. Control Parameters

Coplanar Mode		
	$\boldsymbol{k_p}$	$\boldsymbol{k_i}$
Position	$4\boldsymbol{I}_3$	$0.08\boldsymbol{I}_3$
Orientation	$\begin{bmatrix}5&0&0\\0&5&0\\0&0&2\end{bmatrix}$	$\begin{bmatrix}0.12&0&0\\0&0.12&0\\0&0&0.048\end{bmatrix}$
	$\boldsymbol{k_p}$	$\boldsymbol{k_d}$
Velocity	$3\boldsymbol{I}_3$	$0.4\boldsymbol{I}_3$
Angular Rate	$\begin{bmatrix}9&0&0\\0&9&0\\0&0&4.5\end{bmatrix}$	$\begin{bmatrix}1.2&0&0\\0&1.2&0\\0&0&0.5\end{bmatrix}$
Omni Directional Mode		
	$\boldsymbol{k_p}$	$\boldsymbol{k_i}$
Position	$3\boldsymbol{I}_3$	$0.06\boldsymbol{I}_3$
Orientation	$5\boldsymbol{I}_3$	$0.12\boldsymbol{I}_3$
	$\boldsymbol{k_p}$	$\boldsymbol{k_d}$
Velocity	$2.4\boldsymbol{I}_3$	$0.3\boldsymbol{I}_3$
Angular Rate	$9\boldsymbol{I}_3$	$1.2\boldsymbol{I}_3$

B. *Trajectory Tracking Results*

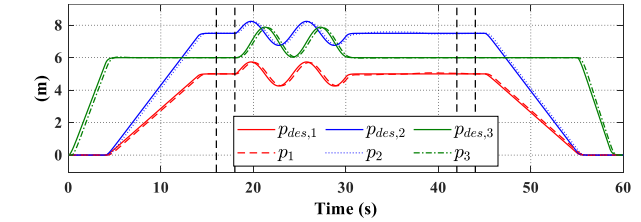

(a) Position Trajectory

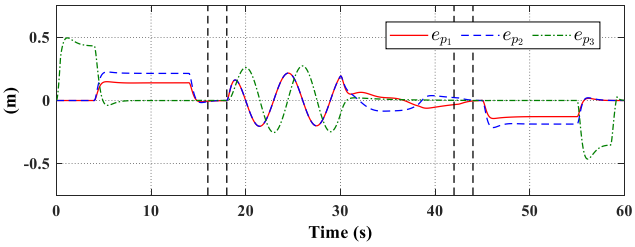

(b) Position Error

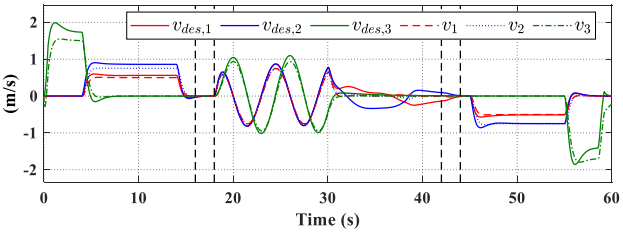

(c) Velocity

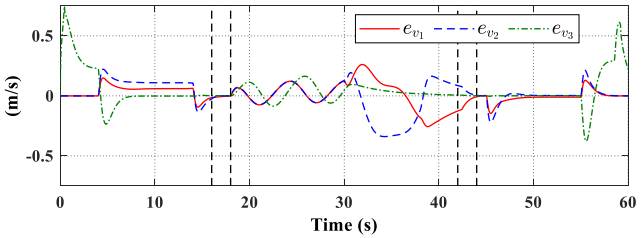

(d) Velocity Error

Fig. 7. Position and Velocity Tracking Results.

Fig. 7 contains the position tracking $\boldsymbol{p} \rightarrow \boldsymbol{p}_{\text{des}}$, the position error $\boldsymbol{e_p}$, the velocity tracking $\boldsymbol{v} \rightarrow \boldsymbol{v}_{\text{des}}$, and the velocity error $\boldsymbol{e_v}$. We select ramping references to represent a high-speed and long-distance motion in the coplanar mode. At the

same time, the maximum position error reaches up to 0.49m, and the maximum velocity error reaches up to 0.74m/s. Sinusoidal references are designed for the position tracking reference of omni mode ($18 \le t < 30$ s). It is worth to note that a fast attitude tracking with steer reference position ($30 \le t < 42$ s) would cause relatively large tracking error. During each transition, the tracking errors are controlled in small ranges ($e_p < 0.001\text{m}, e_v$ <0.02m/s).

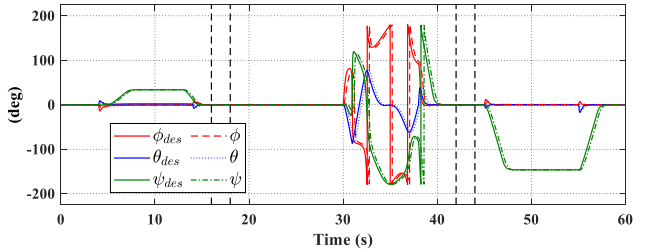

(a) Orientation

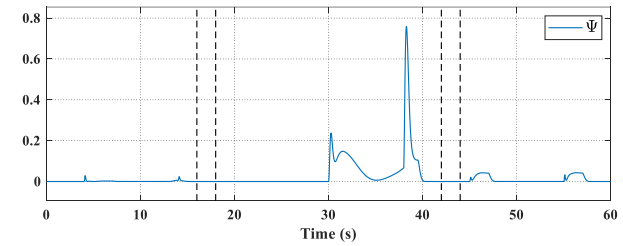

(b) Orientation Tracking Error

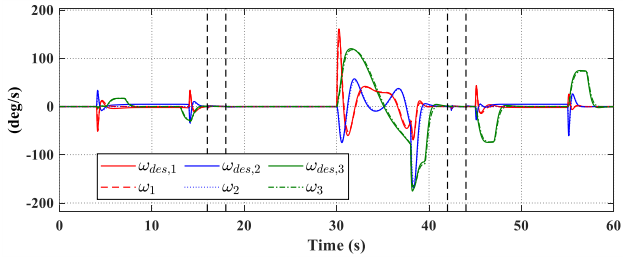

(c) Angular Velocity

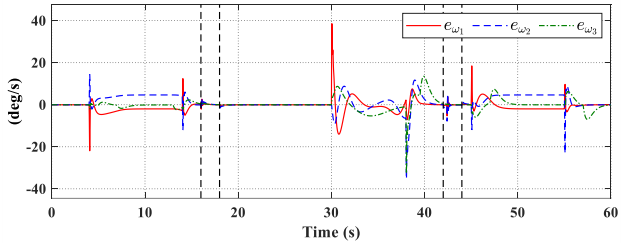

(d) Angular Velocity Error

Fig. 8. Orientation and Angular Velocity Tracking Results.

Moreover, the orientation tracking $\boldsymbol{R} \to \boldsymbol{R}_{\text{des}}$, the orientation tracking error $\Psi(\boldsymbol{R}, \boldsymbol{R}_{\text{des}}) = \frac{1}{2}\text{tr}[\boldsymbol{I} - \boldsymbol{R}_{\text{des}}^T \boldsymbol{R}]$, the angular velocity tracking $\boldsymbol{\omega} \to \boldsymbol{\omega}_{\text{des}}$, and the angular velocity error $\boldsymbol{e}_{\boldsymbol{\omega}}$ are shown in Fig. 8. In the coplanar mode, tracking error is relatively large ($e_{\boldsymbol{R}} < 0.044, e_{\omega} < 23$ deg/s) when changing the heading direction to the targeting area. During $30 \le t < 42$ s, the tracking errors ($e_{\boldsymbol{R}} < 0.77, e_{\omega}$ <38 deg/s) are caused by the UAV fast rotations to adjust roll, pitch, and yaw angles simultaneously (aggressive references). Similar to position tracking, the orientation tracking errors are controlled in small ranges ($e_{\boldsymbol{R}} < 0.44, e_{\omega}$ <0.2 deg/s) during each transition.

C. *Rotor Thrust, Force Efficiency, and Disturbance*

In Fig. 9, all rotors give thrusts within the constraints during the whole flight mission. In the coplanar mode (phases 1&3), $\gamma = 100\%$ corresponds to upward heading directions of all rotors in the body frame. In phase 2, the fully actuated omnidirectional motions with lower force efficiency $57.7\% \le \gamma \le 100\%$ requiring more thrust for each rotor, especially during the steer position part. Hence, the orientation trajectory should cover the red zone in Fig. 4 as much as possible. It is also worth noting that the internal disturbance torque ($\|\tau_s\| \le 0.0053\text{N} \cdot \text{m}$) at the beginning and the end of each transition time has little influence on orientation tracking ($e_{\boldsymbol{R}} < 0.002, e_{\omega} < 6.4$ deg/s), which shows the effectiveness of the switching control design.

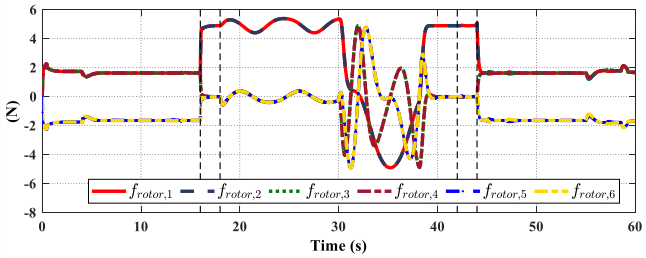

(a) Rotor Thrust

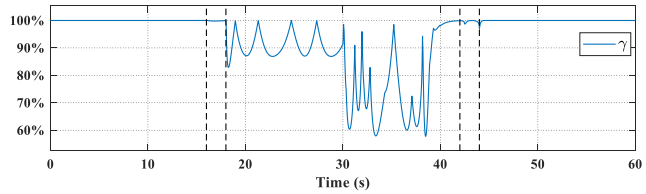

(b) Force Efficiency Index

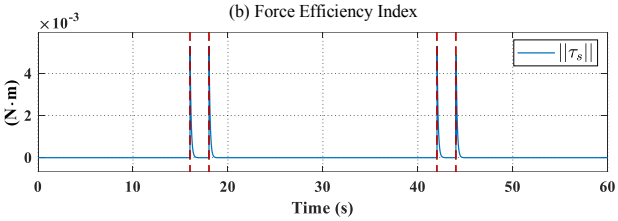

(c) Internal Diturbance Torque

Fig. 9. Rotor Thrust, Force Efficiency, and Internal Disturbance Toque.

D. *Comparison with Coplanar-only and Omni-only UAVs*

Compared with coplanar-only UAVs, it is straightforward that the transformable UAV has omnidirectional flight capability. The transformable UAV does not require other robot arms for many aerial manipulation tasks or only needs less complicated modules to fulfill the same mission [15]-[17]. To compare with omni-only UAVs, the electrical power consumption is calculated (10). Ignoring the power cost of non-rotor modules (flight controller, servo, etc.), we have

$$P \cong \sum_{i=1}^{6} P_{\text{rotor,i}}. \tag{31}$$

An omni-only UAV with a fixed frame is modeled to do the same task as the simulation scenario above. The omni-only UAV flies with $\gamma = 100\%$ (roll and pitch angles are zero) at phases 1 and 3.

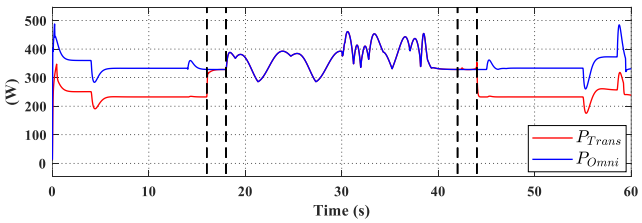

Fig. 10. Power Consumption Comparison.

In Fig. 10, the omni-only UAV costs more electrical power during phases 1&3 than the transformable UAV, performing the same flight mission. The total energy cost of the omni-only UAV is 21134J, and that of the transformable UAV is 17782J.

V. Conclusion and Future Works

The design and characteristics of a transformable UAV combining both coplanar and omnidirectional flight features are shown in this paper. The transformable UAV is proposed to perform both under-actuated coplanar flight and fully actuated omnidirectional motions. A controller with a cascade structure on $\mathbb{R}^3 \times SO(3)$ is designed to achieve the proposed flight capability via different modes considering disturbances. Future work will mainly contain the development of a transformable UAV prototype and validate the proposed design, controller, and desired strengths experimentally.

References

[1] V. Kumar, and N. Michael "Opportunities and challenges with autonomous micro aerial vehicles." *The International Journal of Robotics*, vol. 31, no. 11, pp. 1279–1291, 2012.

[2] A. Idries, N. Mohamed, I. Jawhar, F. Mohamed, and J. Al-Jaroodi, "Challenges of developing UAV applications: A project management view," *2015 International Conference on Industrial Engineering and Operations Management (IEOM)*, pp. 1-10, 2015.

[3] Y. Huang, M. Elli, J. Weast, Y. Lou, S. Lu, and Y. Chen, "RSS model calibration and evaluation for AV driving safety based on naturalistic driving data," Proceedings of *2021 Modeling, Estimation, and Control Conference*, (Invited Paper), IFAC PapersOnLine Vol. 54, Iss. 20, pp. 430-436, 2021.

[4] Y. Huang, F. Wang, A. Li, Y. Shi, and Y. Chen, "Development and performance enhancement of an over-actuated autonomous ground vehicle," *IEEE/ASME Transactions on Mechatronics*, Vol. 26, Iss. 1, pp. 33-44, 2021.

[5] M. Ryll, H. Bülthoff, and P. Giordano, "A novel overactuated quadrotor UAV: modeling, control, and experimental validation," *IEEE Transactions on Control Systems Technology*, vol. 23 no. 2, pp.540-556, 2015.

[6] S. Badr, O. Mehrez, and A. E. Kabeel, "A design modification for a quadrotor UAV: modeling, control, and implementation, " *Advanced Robotics*, vol. 33, pp.1-20, 2018.

[7] I. Al-Ali, Y. H. Zweiri, N. AMoosa, T. Taha, J. M. Dias, L. Seneviratne, "State of the art in tilt-quadrotors, modeling, control and fault recovery," *Journal of Mechanical Engineering Science*. vol.234, 2019

[8] A. B. Junaid, A. D. D. C. Sanchez, J. B. Bosch, N. Vitzilaios, and Y. Zweiri, "Design and implementation of a dual-axis tilting quadcopter," *Robotics,* vol. 7, no.4, pp. 65, 2018.

[9] M. Hamandi, F. Usai, Q. Sablé, N. Staub, M. Tognon and A. Franchi. "Survey on aerial multirotor design: a taxonomy based on input allocation," 2020.

[10] F. Şenkul and E. Altuğ, "Modeling and control of a novel tilt — Roll rotor quadrotor UAV," *2013 International Conference on Unmanned Aircraft Systems (ICUAS)*, pp. 1071-1076, 2013.

[11] P. Zheng, X. Tan, B. B. Kocer, E. Yang and M. Kovac, "TiltDrone: a fully-actuated tilting quadrotor platform," *IEEE Robotics and Automation Letters*, vol. 5, no. 4, pp. 6845-6852, 2020.

[12] M. Odelga, P. Stegagno, and H. H. Bülthoff, "A fully actuated quadrotor UAV with a propeller tilting mechanism: modeling and control, " *2016 IEEE International Conference on Advanced Intelligent Mechatronics*, pp. 306-311, 2016.

[13] D. Brescianini and R. D'Andea, "Design, modeling, and control of an omni-directional aerial vehicle," in *2016 IEEE Int. Conf. on Robotics and Automation*, 2016.

[14] M. Hamandi, K. Sawant, M. Tognon and A. Franchi. "Omni-Plus-Seven (O7+): an omnidirectional aerial prototype with a minimal number of unidirectional thrusters," *2020 International Conference on Unmanned Aircraft Systems (ICUAS)*, pp. 754-761, 2020.

[15] K. Bodie, Z/ Taylor, M. S. Kamel, and R. Siegwart, "Towards efficient full pose omnidirectionality with overactuated MAVs," *Proceeding of the 2018 International Symposium on Experimental Robotics*, 2018.

[16] M. Kamel, S. Verling, O. Elkhatib, C. Sprecher, P. Wulkop, Z. Taylor, R. Siegwart and I. Gilitschenski. "Voliro: an omnidirectional hexacopter with tiltable rotors," ArXiv abs/1801.04581, 2018.

[17] M. Allenspach, K. Bodie, M. Brunner, L. Rinsoz, Z. Taylor, M. Kamel, R. Siegwart and J. Nieto, "Design and optimal control of a tiltrotor micro-aerial vehicle for efficient omnidirectional flight," *The International Journal of Robotics Research*, no. 10-11, pp. 1305-1325, 2020.

[18] D. A. Ta, I. Fantoni, and R. Lozano, "Modeling and control of a tilt tri-rotor airplane," *American Control Conference*, pp. 131–136, 2012.

[19] R. D'Sa, D. Jenson, T. Henderson, J. Kilian, B. Schulz, M. Calvert, T. Heller, and N. Papanikolopoulos. "SUAV:Q - An improved design for a transformable solar-powered UAV," *2016 IEEE/RSJ International Conference on Intelligent Robots and Systems (IROS)*, pp. 1609–1615, 2016.

[20] M. Ryll, D. Bicego and A. Franchi, "Modeling and control of FAST-Hex: A fully-actuated by synchronized-tilting hexarotor, " *IEEE/RSJ International Conference on Intelligent Robots and Systems (IROS)*, pp. 1689-1694, 2016.

[21] IQ Motor (2022). https://www.iq-control.com/vertiq-2306-2200kv. Accessed Feb 14, 2021.

[22] M. Allenspach, K. Bodie, M. Brunner, L. Rinsoz, Z. Taylor, M. Kamel, R. Siegwart, and J. Nieto. "Design and optimal control of a tiltrotor micro-aerial vehicle for efficient omnidirectional flight." *The International Journal of Robotics*, vol. 39, no. 10–11, pp. 1305–1325, Sept. 2020.

[23] T. Lee, M. Leok, and N. H. McClamroch, "Geometric tracking control of a quadrotor UAV on SE(3)," *49th IEEE Conference on Decision and Control (CDC)*, pp. 5420-5425, 2010.

[24] Y. Yu, S. Yang, M. Wang, C. Li, and Z. Li, "High performance full attitude control of a quadrotor on SO(3)," *IEEE International Conference on Robotics and Automation (ICRA)*, pp. 1698-1703, 2015.

[25] R. R. Warier, A. K. Sanyal, S. Sukumar and S. P. Viswanathan, "Feedback tracking control schemes for a class of underactuated vehicles in SE(3)," *American Control Conference (ACC)*, pp. 899-904, 2017.

[26] S. P. Bhat and D. S. Bernstein, "Lyapunov analysis of finite-time differential equations," *American Control Conference (ACC)*, vol. 3, pp. 1831–1832, 1995.

[27] N. Michael, D. Mellinger, Q. Lindsey and V. Kumar, "The GRASP Multiple Micro-UAV Testbed," in *IEEE Robotics & Automation Magazine*, vol. 17, no. 3, pp. 56-65, Sept. 2010.

[28] T. Madani and A. Benallegue, "Backstepping control for a quadrotor helicopter, " 2006 IEEE/RSJ *International Conference on Intelligent Robots and Systems*, pp. 3255-3260, 2006.

[29] D. Tzoumanikas, F. Graule, Q. Yan, S. Dhruv, M. Popovic, S. Leutenegger, "Aerial manipulation using hybrid force and position NMPC applied to aerial writing," arXiv preprint arXiv:2006.02116, 2020.